ACS OMEGA

Article

Cite This: ACS Omega 2018, 3, 12089−12098

http://pubs.acs.org/journal/acsodf

Surface Patterning with SiO_2@PNiPAm Core−Shell Particles

Jo Sing Julia Tang,[†,§] Romina Sigrid Bader,[†,§] Eric S. A. Goerlitzer,[†] Jan Fedja Wendisch,[‡] Gilles Remi Bourret,[‡] Marcel Rey,[†] and Nicolas Vogel*[,†]

[†]Institute of Particle Technology, Friedrich-Alexander University Erlangen-Nürnberg, Cauerstrasse 4, 91058 Erlangen, Germany

[‡]Department of Chemistry and Physics of Materials, University of Salzburg, Jakob Haringer Strasse 2A, A-5020 Salzburg, Austria

Supporting Information

ABSTRACT: Colloidal lithography is a cost-efficient method to produce large-scale nanostructured arrays on surfaces. Typically, colloidal particles are assembled into hexagonal close-packed monolayers at liquid interfaces and deposited onto a solid substrate. Many applications, however, require non close-packed monolayers, which are more difficult to fabricate. Preassembly at the oil/water interface provides non close-packed colloidal assemblies but these are difficult to transfer to a solid substrate without compromising the ordering due to capillary forces acting upon drying. Alternatively, plasma etching can reduce a close-packed monolayer into a non close-packed arrangement, however, with limited interparticle distance and compromised particle shape. Here, we present a simple alternative approach toward non close-packed colloidal monolayers with tailored interparticle distance, high order, and retained spherical particle shape. We preassemble poly(*N*-isopropylacrylamide)-silica (SiO_2@PNiPAm) core−shell particles at the air/water interface, transfer the interfacial spacer to a solid substrate, and use the polymer shell as a sacrificial layer that can be thermally removed to leave a non close-packed silica monolayer. The shell thickness, cross-linking density, and the phase behavior upon compression of these complex particles at the air/water interface provide parameters to precisely control the lattice spacing in these surface nanostructures. We achieve hexagonal non close-packed arrays of silica spheres with interparticle distances between 400 and 1280 nm, up to 8 times their diameter. The retained spherical shape is advantageous for surface nanostructuring, which we demonstrate by the fabrication of gold nanocrescent arrays via colloidal lithography and silicon nanopillar arrays via metal-assisted chemical etching.

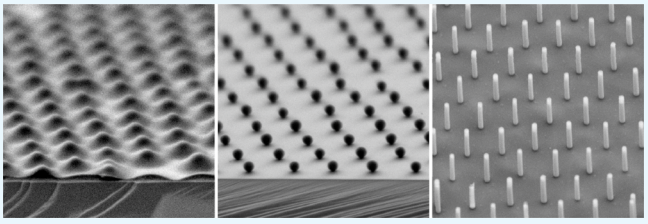

1. INTRODUCTION

Colloidal lithography is a simple, cost-efficient, and scalable method for nanostructuring of surfaces. The process uses spherical colloidal particles as shadow masks to fabricate arrays of complex-shaped nanostructures by angular metal deposition and etching steps.[1−6] The crucial step to prepare surface nanostructure arrays with high precision is the deposition of a colloidal monolayer onto the solid substrate.[7,8] Frequently used methods include the self-assembly at liquid interfaces, followed by deposition on a solid substrate,[9−12] spin-coating,[13] or evaporation-driven self-assembly.[14−19] The simplicity of the method and the control over feature sizes enable applications in various research fields including photonics,[20−23] plasmonics,[5,24−27] phononics,[28−30] electronics,[31−34] anti-reflectivity,[35,36] or the design of liquid-repellent coatings.[37−40]

For maximal flexibility in the lithography process, it is desirable to control the interparticle distance between the individual colloidal particles. The assembly of such non close-packed colloidal monolayers requires either deposition of individual, separated particles directly onto a surface or engineering spacing from an initially close-packed colloidal monolayer. Non close-packed monolayers spontaneously form at the oil/water interfaces due to a more pronounced repulsive character of the constituent colloidal particles.[41] However, their transfer to a solid substrate is substantially more difficult, as immersion capillary forces[42] tend to move particles toward each other.[43] A close-packed monolayer deposited on a flexible substrate can be mechanically separated into a desired lattice structure, but requires an additional transfer step to the target surface and careful control of the involved adhesion energies.[44] Finally, plasma-assisted etching of polymer particles can isotropically shrink the polymer colloidal particles and therefore produce non close-packed monolayers from initially close-packed arrangements.[12,36,45] Although simple to implement, this fabrication method has some limitations. (i) The diameter of the spheres and the spacing are always coupled. By adjusting the etching time, one can either achieve small feature sizes that are highly separated or larger feature sizes with small separations. (ii) The separation between the particles is limited. Typically, polystyrene colloidal particles disintegrate when shrunk to more than half of their diameter. (iii) The morphology of the particles is altered in the etching process. The particles acquire a lens shape and may end up with a wrinkled surface.

A conceptual alternative consists in the assembly of core−shell particles, where the shell can serve as a spacer to separate

Received: August 10, 2018
Accepted: September 12, 2018
Published: September 27, 2018

DOI: 10.1021/acsomega.8b01985
ACS Omega 2018, 3, 12089−12098

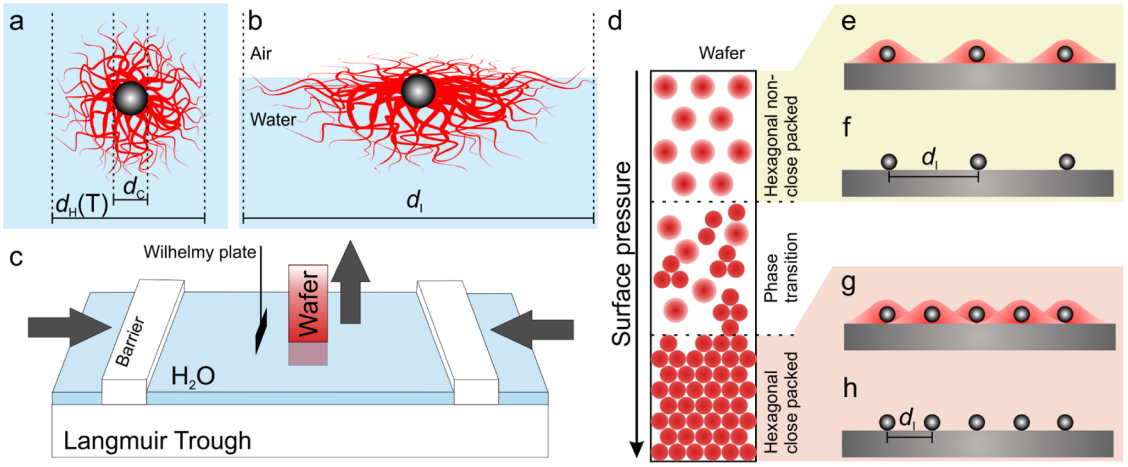

Figure 1. Schematic experimental overview of the self-assembly and surface patterning with SiO_2@PNiPAm core−shell particles. Schematic illustration of the particle geometry in bulk (a) and adsorbed at the air/water interface (b). (c) Schematic of the simultaneous compression and deposition technique on a Langmuir trough.[53] (d) Illustration of the phase diagram of the interfacial assembly transferred to the solid substrate. (e−h) Surface nanopatterning with controlled interparticle spacing by combustion of the organic shell material.

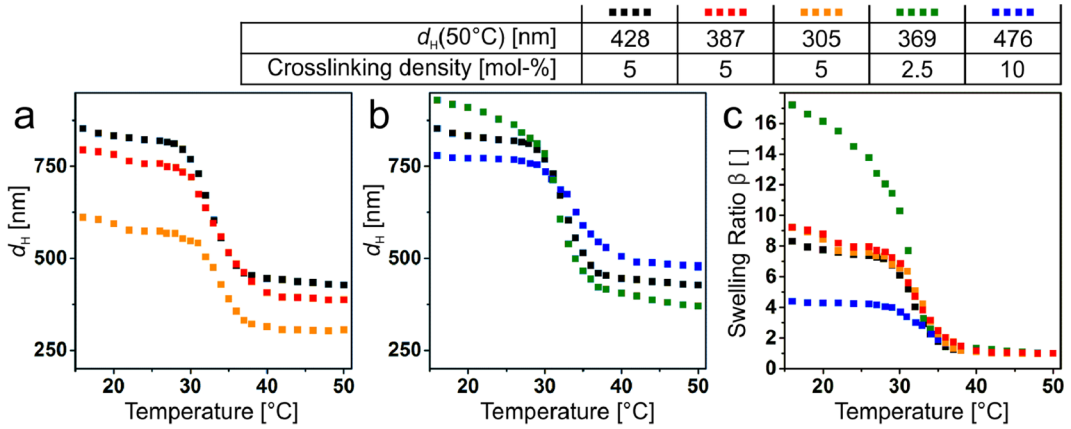

Figure 2. Characterization of the SiO_2@PNiPAm core−shell particles (d_c = 160 nm) with varying shell thicknesses and cross-linking densities: Temperature-dependent hydrodynamic diameter (d_H) measured by DLS for different shell thicknesses (a) and cross-linking densities (b). (c) Swelling ratio β of the SiO_2@PNiPAm core−shell particles. We notice a strong dependence of the cross-linking density on the swelling behavior, whereas the shell thickness had no effect on the swelling behavior.

the core particles. This concept is especially attractive for hybrid organic/inorganic particles, where the shell can be combusted to leave a non close-packed array of inorganic particles on the substrate. For example, using gold core, poly(*N*-isopropylacrylamide) (PNiPAm) shell particles (Au@PNiPAm), nonc lose-packed arrays of gold nanoparticles have been fabricated.[46,47]

Importantly, microgels such as PNiPAm swell in water and are therefore able to deform at a liquid interface and form a characteristic "fried egg" or "core−corona" shape.[48−51] Due to their compressible nature, such microgel particles show a complex interfacial phase behavior as a function of the available interfacial area, which can be systematically varied using a Langmuir trough.[52−56] At low densities, hexagonal non close-packed phases with a corona−corona contact prevail. With decreasing available surface, the system undergoes a phase transition into a hexagonal close-packed phase, where the microgels are in a core−core contact.[48,50,53,54,56,57] The surface pressure upon which the microgels undergo phase transition depends on the cross-linking density.[54,56] Softer, less cross-linked microgels undergo phase transition at higher surface pressures compared to more cross-linked microgels. It was recently shown that SiO_2@PNiPAm core−shell particles undergo similar phase transition from a non close-packed to a close-packed phase.[58,59] This phase behavior, however, was sensitive to the size of the core. The core−shell particles with larger silica cores (d = 360 nm) were not stable at the oil/water interface and aggregated even at low-area fractions.[60]

In this article, we take advantage of the complex phase behavior of SiO_2@PNiPAm core−shell particles and the possibility to remove the organic shell to prepare non close-packed silica colloidal monolayers with high-order and well-controlled interparticle distances. We first study the phase behavior of the hybrid particles at the air/water interface as a function of their physicochemical properties, including the cross-linking density and the relative size ratios. Then, we identify regions of uniform structural arrangements (i.e., outside the surface pressure region where the system undergoes a phase transition) and transfer the interfacial assembly to solid substrates. After shell combustion, we obtain hexagonal non close-packed arrays of spherical silica particles with interparticle distances up to 8 times the core diameter and use these particle arrays to prepare high-quality nanostructures by colloidal lithography.

DOI: 10.1021/acsomega.8b01985
ACS Omega 2018, 3, 12089−12098

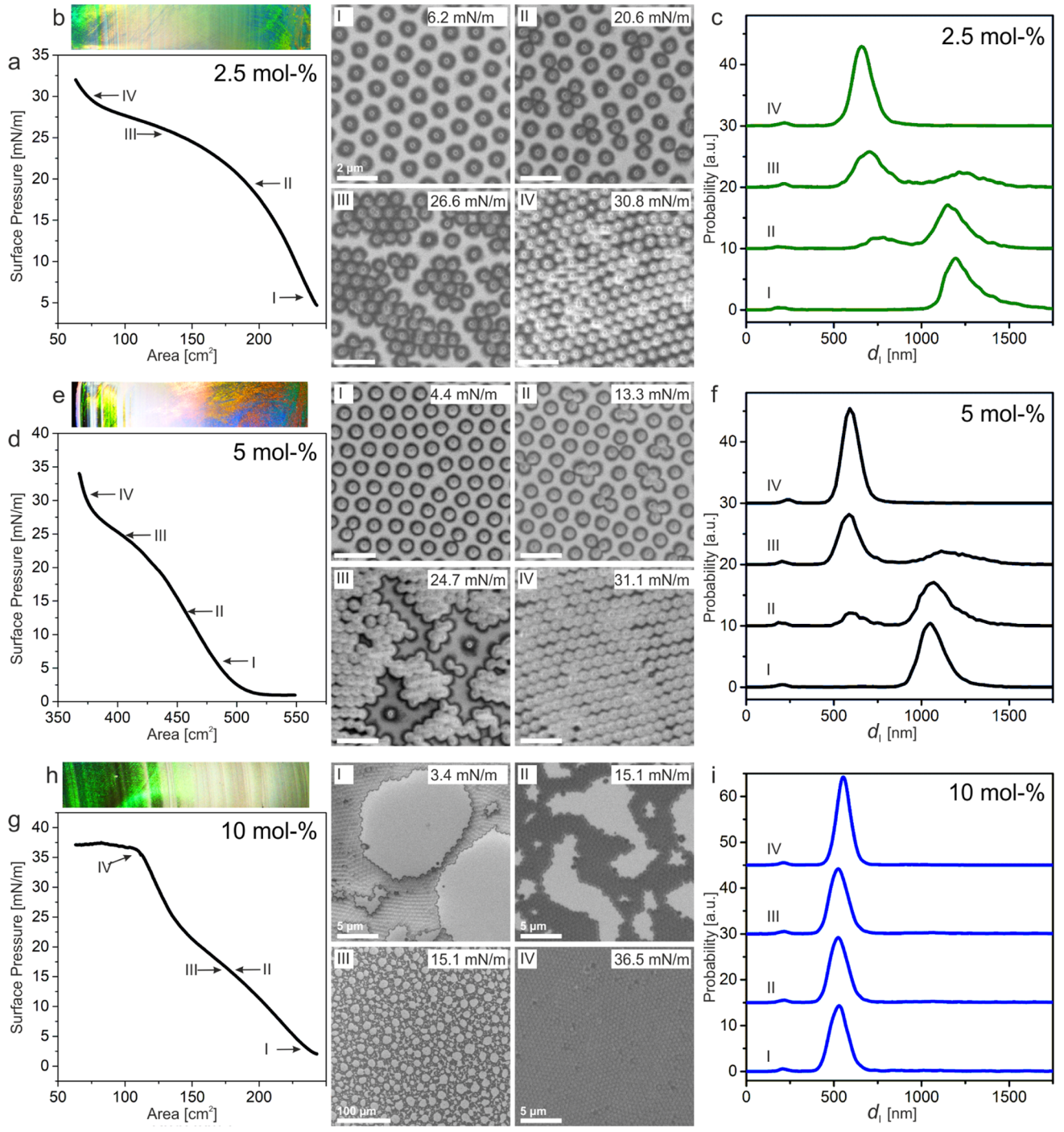

Figure 3. Influence of shell cross-linking density on the interfacial phase behavior of SiO_2@PNiPAm core−shell particles: (a−c) 2.5 mol %, (e−f) 5 mol %, and (g−i) 10 mol %. (a, d, and g) Surface pressure−area isotherm recorded on a Langmuir trough. (b, e, and h) Optical image of the deposited particle array on a silicon wafer. The regions correspond to the compression isotherm in (a, d, and g), displaying the structural colors of the hexagonal non close-packed and close-packed phase connected by the whitish phase transition region. The Roman numbers label represent the SEM images of the observed phases. Scale bars for 2.5 and 5 mol %: 2 μm. (c, f, and i) Interparticle distance distribution of the different phases labeled by the Roman numbers showing the nucleation of a second hexagonal phase.

2. RESULTS AND DISCUSSION

We synthesized SiO_2@PNiPAm core−shell particles by seeded precipitation polymerization.[58,61] We kept the silica core diameter constant (d_c = 160 nm) and varied the PNiPAm shell thickness (Figure 1a) as well as the cross-linking density, which affects the deformability at the liquid interfaces (Figure 1b). We investigated the effect of these physiochemical parameters on the self-assembly at the air/water interface by the simultaneous compression and deposition method,[52−54,58] as schematically illustrated in Figure 1c. This method enables us to continuously transfer the interfacial arrangement of the core−shell particles onto a tilted solid substrate with a fixed angle (Figure 1d). Each position on the wafer can thus be correlated to the corresponding surface pressure. We characterized the gradient on the substrate by scanning electron microscopy (SEM) and statistical image analysis.

DOI: 10.1021/acsomega.8b01985
ACS Omega 2018, 3, 12089−12098

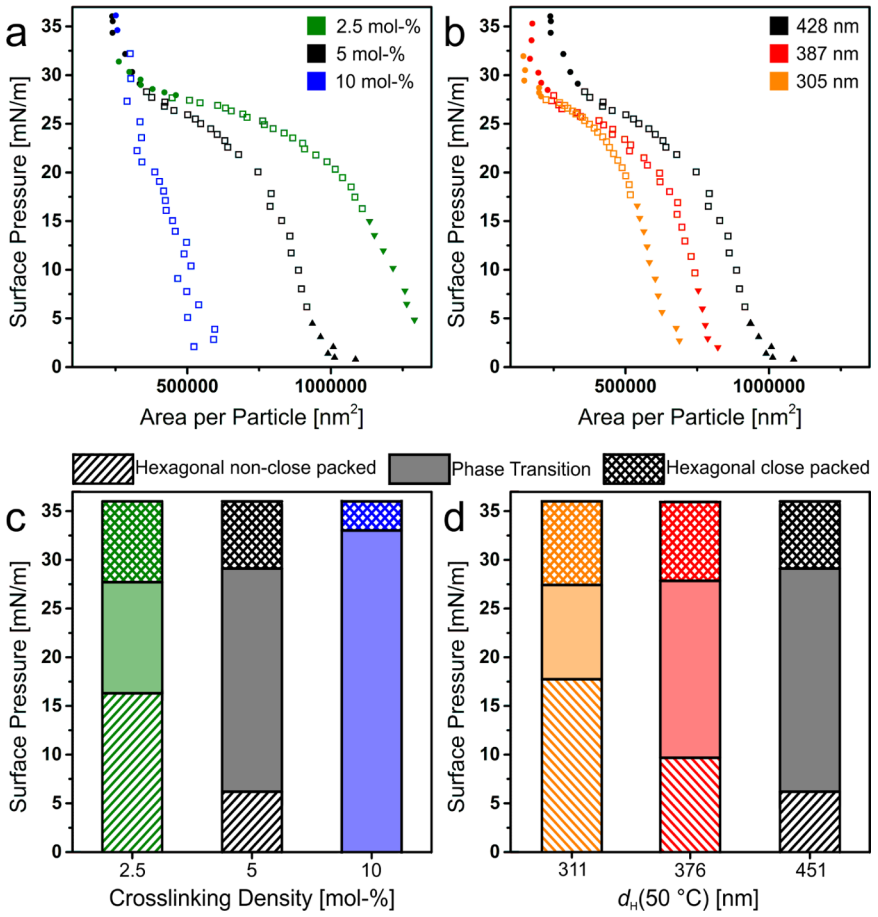

Figure 4. Phase behavior of SiO_2@PNiPAm core−shell particles at the air/water interface. Surface pressure vs measured area per particle isotherm of SiO_2@PNiPAm core−shell particles with different cross-linking densities (a) and different shell diameters (b). Each point corresponds to an area per particle measurement determined by the image analysis of the SEM images after deposition. The triangles represent the hexagonal non close-packed phase, the squares the phase transition, and the dots correspond to the hexagonal close-packed phase. Comparison of the interfacial phases of SiO_2@PNiPAm core−shell particles with different cross-linking densities (c) and different shell diameters (d) as a function of the surface pressure. We notice a dependence of the stability of the hexagonal non close-packed phase on the cross-linking density (c). Further, the phase transition shifts to higher surface pressure values with decreasing shell thickness (d).

Finally, we combusted the shell of the core−shell particles to achieve a non close-packed assembly of the spherical silica cores, which serve as a mask for nanostructuring (Figure 1e−h). We can thus tune the interparticle distance (d_i) by either compression of the air/water interface or by tuning the size and cross-linking density of the PNiPAm shell.

First, we characterized the volume phase transition[62] and the corresponding particle dimensions in bulk using temperature-dependent dynamic light scattering (DLS) (Figure 2). In the first set of particles, we kept the cross-linking density constant at 5 mol % and varied the shell thickness by increasing the ratio of monomer to SiO_2 cores (Figure 2a), providing particles with a total diameter from 305 to 428 nm in the collapsed state at 50 °C. In the second set of particles, we fixed the monomer-to-SiO_2 ratio and varied the cross-linking density (Figure 2b), which influences the temperature-dependent swelling behavior of the microgel shell. To characterize the swelling behavior, we defined the swelling ratio β

$$\beta = V_S(T)/V_S(50\ ^\circ\mathrm{C}) \quad (1)$$

where $V_S(T)$ is the volume of the shell without the core and $V_S(50\ ^\circ\mathrm{C})$ is the volume of the shell in the collapsed state measured at 50 °C. As expected, the cross-linking swelling behavior decreases with increasing cross-linking density (Figure 2c).[54,56] The shell thickness, however, has no effect on the swelling behavior, which is in agreement with previous work.[58]

Next, we investigated the influence of the cross-linking density on the interfacial phase behavior of the core−shell particles at the air/water interface on a Langmuir trough. We transferred the interfacial arrangement of the core−shell particles to a silicon wafer by simultaneous compression and deposition. We then systematically analyzed the substrate with a gradient length of 34 mm by taking a scanning electron microscopy (SEM) image each millimeter. Each image was analyzed by statistical image analysis based on the publicly available Matlab version of the IDL code by Crocker and Grier.[63] Figure 3 shows the phase behavior of the core−shell particles with 2.5 mol % cross-linker (Figure 3a−c), 5 mol % cross-linker (Figure 3d−f), and 10 mol % cross-linker (Figure 3g−i). For the core−shell particles with 2.5 and 5 mol % cross-linking density, we observed a stable hexagonal non close-packed phase at low surface pressures (Figure 3I). Upon increasing the surface pressure, the core−shell particles underwent a phase transition into a hexagonal close-packed phase (Figure 3II,III) until all the core−shell particles were in the close-packed phase (Figure 3IV). The phase transition can be characterized by the interparticle distance distribution

DOI: 10.1021/acsomega.8b01985
ACS Omega 2018, 3, 12089−12098

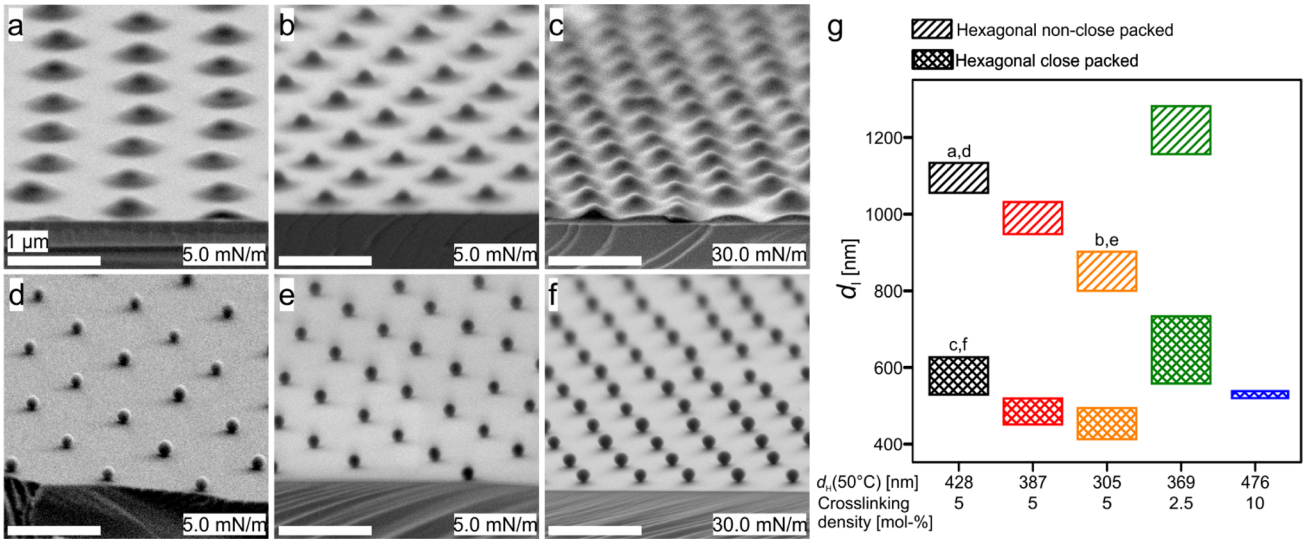

Figure 5. Non close-packed silica monolayers from deposited SiO_2@PNiPAm core−shell particles. Representative tilted SEM images of the SiO_2@PNiPAm core−shell particles deposited at surfaces pressures of 5 mN/m (a, b, d, and e) and at 30 mN/m (c, f) before (a, b, and c) and after shell combustion (d, e, and f). All scale bars: 1 μm. (g) Interparticle distances obtained for the core−shell particles with various diameters (d_H(50 °C)) and cross-linking densities ranging from 1150 to 410 nm. The labels (a)−(f) correspond to the SEM images.

(Figure 3c,f), where we observe the growth of the second hexagonal close-packed phase. The phase behavior is similar to previous work on SiO_2@PNiPAm core−shell particles[58] and PNiPAm microgels with an internal core−shell structure.[53]

However, the phase behavior changed for the core−shell particles with 10 mol % cross-linking density. In this sample, we did not observe a stable hexagonal non close-packed phase, and the particles directly aggregated into a hexagonal close-packed phase containing voids (Figure 3I). These voids gradually disappeared upon compression until a complete hexagonal close-packed monolayer was observed at a surface pressure above 30 mN/m (Figure 3IV). This behavior is reflected by the analysis of the interparticle distance distribution, where we did not detect any changes in the interparticle distance regardless of the surface pressure during transfer (Figure 3i). The phase transition can also be seen directly by the macroscopic optical appearance of the interfacial layer deposited onto the silicon wafer substrates (Figure 3b,e,h). The ordered hexagonal close-packed and non close-packed regions show prominent structural colors resulting from grating diffraction at the ordered colloidal lattice, whereas the phase transition region appears white due to the disordered assembly.[64]

We also analyzed the phase diagram of the core−shell particles with a fixed cross-linking density and different shell thickness. For the core−shell particles with 5 mol % cross-linking density, we found a stable hexagonal non close-packed phase, a phase transition region, and a hexagonal close-packed phase, with different interparticle distances as expected from the different shell thicknesses (Figure S1). We assume that capillary forces during drying do not change the assembly, as we observe non close-packed structures, which coincide with direct observation at the oil/water interface.[48,58] If capillary forces were strong enough to alter the assembly, these non close-packed structures would collapse into close-packed structures.

We used the statistical image analysis to compare the compression isotherms of the different core−shell particles and to quantify the resulting monolayer structure (Figure 4). We calculated the area per particle by dividing the area of each SEM by the number of microgel particles. Figure 4a,b shows the surface pressure−area per particle isotherm for different cross-linking densities (Figure 4a) and different shell thickness (Figure 4b). Each dot corresponds to the area per particle analyzed from the SEM images. We observed a dependence of the cross-linking density on the spreading of the SiO_2@PNiPAm particles with similar shell thickness at the air/water interface (Figure 4a). With decreasing cross-linking density, the particles are able to spread more at the air/water interface and thus occupy larger areas, in agreement with previous work.[54,56] At high surface pressure (>30 mN/m), all particles show a similar area per particle of 250 000 nm^2, which corresponds to an interparticle distance of 564 nm. This is substantially larger than the silica core with a diameter d_c = 160 nm. Thus, even in the most compressed, close-packed region, the silica cores are separated by the PNiPAm shell. For different shell thicknesses, we observed a similar shape in the surface pressure−area per particle isotherm, but with a shift to a lower area per particle, and thus core separations, for thinner shells (Figure 4b).

The cross-linking density and the shell thickness also influenced the phase transition (marked as squares in Figure 4a,b and filled region in Figure 4c,d). The phase transition shifted to higher surface pressure for lower cross-linking densities, in agreement with previous work on microgels (Figure 4c).[54] For 10 mol % cross-linking density, the core−shell particles directly underwent phase transition and aggregated even below 1 mN/m. A similar behavior was observed for core−shell particles with a larger silica core.[60] We hypothesize that with increasing cross-linking density, the size of the corona decreases and is not able to overcome the attractive capillary interactions between the particle cores. Interestingly, the shell thickness also influenced the start of the phase transition (Figure 4d). The phase transition shifted to higher surface pressures for smaller shell thicknesses, which is the opposite behavior compared to previous work by Rauh et al.,[58] where a larger shell led to a better stabilization of the core−shell particles at the air/water interface and thus a higher

DOI: 10.1021/acsomega.8b01985
ACS Omega 2018, 3, 12089−12098

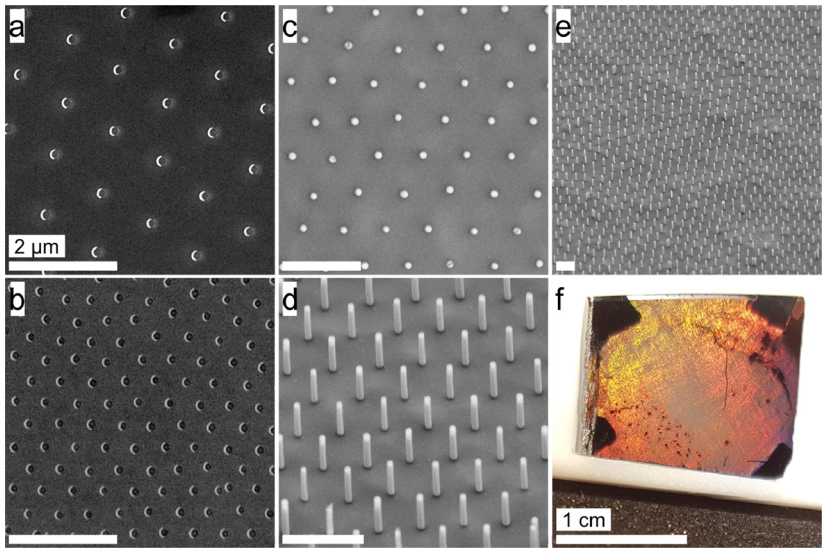

Figure 6. Applications of non close-packed silica monolayers as templates in colloidal lithography. (a, b) SEM images of Au nanocrescents with different spacings ((a) 1100 nm; (b) 600 nm) but constant dimensions of 160 nm. (c–f) Vertically aligned silicon nanowires etched by metal-assisted chemical etching (MACE). (c) Top view image showing the hexagonal symmetry inherited from the colloidal monolayer template. (d, e) Side-view images tilted by 30°. Scale bars: 2 μm. (f) Macroscopic photograph of the etched silicon wafer. Regions with silicon nanowires show structural coloration. The dark edges correspond to the areas where the substrate was fixed to the stage of the metal evaporator. Scale bar: 1 cm.

surface pressure at the phase transition. We believe that this behavior is due to differences in the sizes of the core–shell particles. In the work by Rauh et al., the particles were significantly smaller compared to the particles in the present study (the largest core–shell particles had a collapsed diameter of d_H(40 °C) = 250 nm, whereas our smallest core–shell particle had a collapsed diameter of d_H(40 °C) = 305 nm). The differences in the phase behavior can be ascribed to the interfacial deformations induced by the PNiPAm shells of different thickness and cross-linking ratio. We further hypothesize that only the outer part of the PNiPAm shell governs the properties of the corona and thus expands the core–shell particle at the air/water interface.

The phase diagram then provided us with design criteria to prepare non close-packed colloidal monolayers. Long-range order and controlled lattice spacing can be obtained for interfacially assembled core–shell particles transferred to a solid substrate before or after the phase transition, i.e., in the hexagonal non close-packed and the close-packed phase. Figure 5a–c shows the tilted SEM images of the SiO_2@PNiPAm core–shell particles at low (Figure 5a,b) and high surface pressures (Figure 5c). We notice that even in the hexagonal close-packed phase, the silica cores are still separated by their PNiPAm shell. After thermal combustion of the polymeric shell, we yield well-ordered nonclose-packed arrangements of the silica spheres (Figure 5d–f). Figure 5g provides an overview of the obtainable interparticle distances from the set of samples within this study. By variation in the shell thickness and the cross-linking densities, the interparticle distance can be continuously adjusted between 400 and 1280 nm.

Finally, we demonstrate the potential of the prepared non close-packed colloidal monolayers in two typical applications of colloidal lithography. First, we prepared arrays of gold nanocrescents[5,26] (Figure 6a,b). We thermally evaporated a thin gold film (30 nm) onto the colloidal monolayer mask with a substrate tilt angle of 30° and subsequently used reactive ion etching at normal incidence to remove the gold film from the substrate. Gold only remains on the surface in areas shielded by the colloidal particles, giving rise to crescent-shaped nanostructures. In Figure 6a,b, we can see the advantage of using core–shell particles to prepare the colloidal shadow mask. The spacing between the particles, and thus between the nanocrescents, can be adjusted precisely and over a wide range. Additionally, the silica particles completely retain their spherical shape, leading to nanocrescents with defined contour and sharp tips. In contrast, crescent arrays fabricated with plasma-etched colloidal monolayers as masks feature much rougher contours as the colloidal particles are partially degraded during the etching process.[65]

As a second nanostructuring process, we prepared arrays of vertically aligned silicon nanowires from metal-assisted chemical etching (Figure 6c–f).[22,23,66–68] We first created a metal nanohole array by thermally evaporating gold through the non close-packed colloidal monolayer. The gold film then serves as a catalyst in the metal-assisted chemical etching step, in which hydrofluoric acid and hydrogen peroxide are used to dissolve the silicon underneath the gold film. As a result, arrays of silicon nanopillars are obtained (Figure 6c–f). The nanowires are uniform in size and show a smooth and perfectly round shape due to the well-defined spherical shape and smooth surface of the silica particles forming the nonclose-packed monolayer. The silicon nanowire array shows vivid structural colors due to the regular spacing between the individual nanowires over macroscopic dimensions (Figure 6f).

3. CONCLUSIONS

In this article, we investigated the interfacial behavior of SiO_2@PNiPAm core–shell particles under compression on a Langmuir trough. We found that these hybrid particles undergo a phase transition from a non close-packed arrangement with a corona–corona contact to a close-packed arrangement with collapsed microgel shells in direct contact. The surface pressure required for this phase transition depended on both the cross-linking density and the thickness of the microgel shell. Importantly, both before and after the

DOI: 10.1021/acsomega.8b01985
ACS Omega 2018, 3, 12089–12098

phase transition region, the hybrid particles formed well-ordered arrangements that could be transferred to a solid substrate. After combustion of the microgel shell, arrays of non close-packed silica particles can thus be obtained with high precision. The spreading of the microgel shell enabled a wide separation of the silica cores without compromising the order. Using our set of microgel particles, the interparticle distance could be tailored between 400 and 1280 nm. In contrast to the existing methods to prepare nonclose-packed colloidal monolayers, our method enabled a precise control of the interparticle distance over a wide range, a choice of the core size independent of the lattice spacing, and perfect spherical shapes and long-range order of the particles in the non close-packed monolayer.

These characteristics provide ideal conditions for applications in colloidal lithography, which we demonstrate by the fabrication of gold nanocrescents and silicon nanowire arrays.

4. EXPERIMENTAL SECTION

4.1. Materials. All the chemicals were purchased from commercial sources and used as received unless stated otherwise. *N*,*N*′-Methylenebis(acrylamide) (BIS; 99%, Sigma-Aldrich), ammonium persulfate (APS, Sigma-Aldrich, 98%), ethanol (EtOH, Sigma-Aldrich, 99.9%), hexane (≥99%, Sigma-Aldrich), tetraethyl orthosilicate (TEOS; 98%, Sigma-Aldrich), ammonium hydroxide solution (28−30% NH_3 basis, Sigma-Aldrich), (3(trimethoxysilyl)propyl methacrylate) (MPS; 98%, Sigma-Aldrich), fluorescein isothiocyanate isomer I (FITC; Sigma-Aldrich, >90%), (3-aminopropyl)triethoxysilane (APTS; Sigma-Aldrich, >98%), hydrofluoric acid (HF, AnalaR NORMAPUR, VWR, 40%), and hydrogen peroxide (H_2O_2, EMSURE, Merck, 30%) were used as received.

N-Isopropylacrylamide (NiPAm; 97%, Sigma-Aldrich) was purified by recrystallization from hexane (95%, Sigma-Aldrich). Water was double deionized using a Milli-Q system (18.2 MΩ cm, Elga PURELAB Flex).

4.2. Synthesis of Functionalized Silica Nanoparticles. Fluorescent silica nanoparticles with a diameter of 160 nm (±10 nm) were prepared according to the Stöber process.[69] The fluorescent labeling was performed on the basis of the previously reported protocols.[60,70] First, 5.8 mg FITC (1.5×10^{-2} mmol) was dissolved in 1.5 mL EtOH (10 mM). Then, 26.19 μL APTS (1.5×10^{-1} mmol, 10 equiv) was added to the solution. After the mixture was stirred for 2.5 h in the dark, 900 μL of the reaction mixture was diluted with 4.50 mL of EtOH (5 vol equiv).

In a round-bottom flask, 250 mL EtOH, 12.5 mL Milli-Q water, and 25 mL NH_3(aq) were stirred together. TEOS, 18.75 mL, was stirred in 75 mL EtOH and both solutions were heated to 50 °C and equilibrated for 30 min. The TEOS solution was then quickly added to the first mixture under heavy stirring. As soon as the reaction mixture became turbid, the prepared fluorescent dye solution was slowly added within 8 min. We let the reaction proceed for 2 d at 50 °C.

This suspension was used for functionalization without any further purification. We functionalized the fluorescent silica nanoparticles with MPS and calculated its amount to obtain one molecule of MPS per 40 $Å^2$ surface area. The surface area of the silica particles was approximately calculated by determining the mass fraction of the silica dispersion and using a density of 2.0 g/cm^3, not taking the porosity of Stöber particles into account.[71] MPS, 102.7 μL (3.9×10^{-4} mmol), was rapidly added to the silica dispersion. We allowed the reaction mixture to stir at room temperature for at least 1 d and then boiled it for 1 h to ensure successful functionalization. Afterward, we purified the particles by centrifugation and redispersed them three times in ethanol and three times in Milli-Q water. A yellow silica dispersion of 6.59 wt % was obtained.

4.3. Synthesis of SiO_2@PNiPAm Core−Shell Particles. A PNiPAm-microgel shell was polymerized on the synthesized silica nanoparticles via surfactant-free precipitation polymerization. In a round-bottom flask, 282.9 mg of NiPAm (2.5 mmol; 50 mmol/L) and the respective amount of BIS (Table S1) were dissolved in Milli-Q water. Then, we slowly added the prepared silica dispersion under stirring. The mixture was heated to 80 °C and purged with nitrogen. After an equilibration time of 30 min, the nitrogen gas inlet was replaced by a nitrogen-filled balloon to sustain the nitrogen atmosphere. The reaction was started by rapidly adding 114 mg of APS dissolved in 1 mL Milli-Q water. We let the reaction proceed for an hour before quickly adding 114 mg of APS dissolved in 1 mL Milli-Q water again. Subsequently, a nitrogen-purged solution of NiPAm and BIS (Table S2) was added using a syringe pump (3 mL/h; 6 mmol/L) for further shell growth. Two hours after the last addition of the reagents, the reaction mixture was allowed to cool to room temperature. The core−shell particles were purified by centrifugation with Milli-Q water to dispose of free microgel particles and pure silica nanoparticles.

4.4. Langmuir Trough Simultaneous Compression and Deposition. We used the simultaneous compression and deposition method as described in previous work.[52−54,58] We used a Teflon Langmuir trough (KSVNIMA) (area = 243 cm^2, width = 7.5 cm) with Delrin barriers and the surface pressure was measured by a Wilhelmy plate. The N-type silicon wafers (Infineon, resistivity: 0.1−10 Ω cm) were cut to 4×1 cm^2 and cleaned by ultrasonication in ethanol and Milli-Q water, followed by oxygen plasma (Diener). The substrate was mounted in a 45° angle and the trough was filled with Milli-Q water. The core−shell particle suspension was diluted to 0.5 wt % and mixed with 30 wt % ethanol as the spreading agent. The core−shell particles were spread on the air/water interface of the Langmuir trough using a regular 100 μL pipette. After 10 min of equilibration, the barriers were compressed at a speed of 4 mm/min and the substrate was lifted at a speed of 0.8 mm/min. The core−shell particle assembly was further characterized by SEM.

4.5. Statistical Image Analysis. We characterized the phase diagram of the core−shell particles by statistical image analysis based on the publicly available Matlab version of the IDL code by Crocker and Grier.[63] We first removed the PNiPAm shell by oxygen plasma and systematically took an SEM image at each millimeter of the silicon wafer with the deposited assembly using a voltage of 5 kV. We choose a resolution of 2028×1536 $pixel^2$ and a magnification of 2000. Because we deposit with a fixed angle, we were able to correlate each position of the substrate with its corresponding surface pressure. The area per particle was calculated by dividing the area of the image by the number of particles. The nearest neighbor distribution was fitted by two Gauss fits.

4.6. Gold Evaporation/Nanocrescents. The plasmonic nanostructures were produced by following an established colloidal lithography method.[26,65] Oxygen plasma (Diener electric Femto) was used to remove polymer residuals from the core−shell particles and guarantee proper wetting conditions

DOI: 10.1021/acsomega.8b01985
ACS Omega 2018, 3, 12089−12098

of the substrate. Titanium (1 nm, HMW Hauner, 99.995%, <3 mm granulate) was evaporated under a 30° angle with respect to the surface normal as an adhesion layer, subsequently followed by 20 nm gold (HMW Hauner, 99.99%, <3 mm granulate) using a custom-built thermal evaporator (Torr International Inc, THE3-KW). Directed argon etching (Oxford instruments, PlasmaPro NGP 80) along the surface normal was utilized to gain crescent-shaped particles and remove all redundant metallic material not covered by the colloidal shadow. The silica spheres were removed using an adhesive tape.

4.7. Metal-Assisted Chemical Etching. We used metal-assisted chemical etching (MACE) to prepare Si nanowires in a HF/H_2O_2 mixture. Here, we used the silica cores as a mask and evaporated 3 nm titanium as an adhesion layer followed by 20 nm gold, which acts a catalyst for the reduction of H_2O_2 and induces fast anisotropic etching of the Si in the regions covered by the Au metal film. As a result, the metal film sinks in the Si substrate, whereas the areas not covered by the metal are not etched.[66,72]

MACE was performed within a Teflon beaker using a laboratory-made polylactic acid sample holder perforated with small holes. The etching solution was prepared fresh and composed of 10 mL HF, 10 mL Milli-Q water, and 2 mL H_2O_2. The sample was placed on the Teflon holder and immersed in the etching solution for 10 min. Afterward, the sample was rinsed with deionized water three times, rinsed with ethanol once, and dried in air.[22]

■ ASSOCIATED CONTENT

Supporting Information

The Supporting Information is available free of charge on the ACS Publications website at DOI: 10.1021/acsomega.8b01985.

Monomers used for the core−shell particle synthesis; phase diagram of core−shell particles with different shell thickness (PDF)

■ AUTHOR INFORMATION

Corresponding Author

*E-mail: nicolas.vogel@fau.de.

ORCID

Gilles Remi Bourret: 0000-0002-9774-1686

Nicolas Vogel: 0000-0002-9831-6905

Author Contributions

§J.J.T. and R.S.B. contributed equally to this work.

Notes

The authors declare no competing financial interest.

■ ACKNOWLEDGMENTS

The research was supported by the Deutsche Forschungsgemeinschaft (DFG) under grant number VO 1824/6-1. N.V. also acknowledges support by the Interdisciplinary Center for Functional Particle Systems (FPS). G.R.B. and J.F.W. gratefully acknowledge support from the Austrian Science Fund FWF for project P-28797 "Intergranular regions in nanocrystalline ceramics".

■ REFERENCES

(1) Ai, B.; Möhwald, H.; Wang, D.; Zhang, G. Advanced Colloidal Lithography Beyond Surface Patterning. *Adv. Mater. Interfaces* **2017**, *4*, No. 1600271.

(2) Ai, B.; Yu, Y.; Möhwald, H.; Zhang, G.; Yang, B. Plasmonic Films Based on Colloidal Lithography. *Adv. Colloid Interface Sci.* **2014**, *206*, 5−16.

(3) Wang, Z.; Ai, B.; Möhwald, H.; Zhang, G. Colloidal Lithography Meets Plasmonic Nanochemistry. *Adv. Opt. Mater.* **2018**, No. 1800402.

(4) Hulteen, J. C.; Van Duyne, R. P. Nanosphere Lithography: A Materials General Fabrication Process for Periodic Particle Array Surfaces. *J. Vac. Sci. Technol., A* **1995**, *13*, 1553−1558.

(5) Retsch, M.; Tamm, M.; Bocchio, N.; Horn, N.; Förch, R.; Jonas, U.; Kreiter, M. Parallel Preparation of Densely Packed Arrays of 150-Nm Gold-Nanocrescent Resonators in Three Dimensions. *Small* **2009**, *5*, 2105−2110.

(6) Nemiroski, A.; Gonidec, M.; Fox, J. M.; Jean-Remy, P.; Turnage, E.; Whitesides, G. M. Engineering Shadows to Fabricate Optical Metasurfaces. *ACS Nano* **2014**, *8*, 11061−11070.

(7) Vogel, N.; Weiss, C. K.; Landfester, K. From Soft to Hard: The Generation of Functional and Complex Colloidal Monolayers for Nanolithography. *Soft Matter* **2012**, *8*, 4044.

(8) Lotito, V.; Zambelli, T. Approaches to Self-Assembly of Colloidal Monolayers: A Guide for Nanotechnologists. *Adv. Colloid Interface Sci.* **2017**, *246*, 217−274.

(9) Weekes, S. M.; Ogrin, F. Y.; Murray, W. A.; Keatley, P. S. Macroscopic Arrays of Magnetic Nanostructures from Self-Assembled Nanosphere Templates. *Langmuir* **2007**, *23*, 1057−1060.

(10) Sirotkin, E.; Apweiler, J. D.; Ogrin, F. Y. Macroscopic Ordering of Polystyrene Carboxylate-Modified Nanospheres Self-Assembled at the Water-Air Interface. *Langmuir* **2010**, *26*, 10677−10683.

(11) Retsch, M.; Zhou, Z.; Rivera, S.; Kappl, M.; Zhao, X. S.; Jonas, U.; Qin, L. Fabrication of Large-Area, Transferable Colloidal Monolayers Utilizing Self-Assembly at the Air/water Interface. *Macromol. Chem. Phys.* **2009**, *210*, 230−241.

(12) Vogel, N.; Goerres, S.; Landfester, K.; Weiss, C. K. A Convenient Method to Produce Close- and Non-Close-Packed Monolayers Using Direct Assembly at the Air-Water Interface and Subsequent Plasma-Induced Size Reduction. *Macromol. Chem. Phys.* **2011**, *212*, 1719−1734.

(13) Mihi, A.; Ocaña, M.; Míguez, H. Oriented Colloidal-Crystal Thin Films by Spin-Coating Microspheres Dispersed in Volatile Media. *Adv. Mater.* **2006**, *18*, 2244−2249.

(14) Malaquin, L.; Kraus, T.; Schmid, H.; Delamarche, E.; Wolf, H. Controlled Particle Placement through Convective and Capillary Assembly. *Langmuir* **2007**, *23*, 11513−11521.

(15) Prevo, B. G.; Velev, O. D. Controlled, Rapid Deposition of Structured Coatings from Micro- and Nanoparticle Suspensions. *Langmuir* **2004**, *20*, 2099−2107.

(16) Watanabe, S.; Inukai, K.; Mizuta, S.; Miyahara, M. T. Mechanism for Stripe Pattern Formation on Hydrophilic Surfaces by Using Convective Self-Assembly. *Langmuir* **2009**, *25*, 7287−7295.

(17) Mino, Y.; Watanabe, S.; Miyahara, M. T. Fabrication of Colloidal Grid Network by Two-Step Convective Self-Assembly. *Langmuir* **2011**, *27*, 5290−5295.

(18) Born, P.; Blum, S.; Munoz, A.; Kraus, T. Role of the Meniscus Shape in Large-Area Convective Particle Assembly. *Langmuir* **2011**, *27*, 8621−8633.

(19) Born, P.; Munoz, A.; Cavelius, C.; Kraus, T. Crystallization Mechanisms in Convective Particle Assembly. *Langmuir* **2012**, *28*, 8300−8308.

(20) Park, C.; Koh, K.; Jeong, U. Structural Color Painting by Rubbing Particle Powder. *Sci. Rep.* **2015**, *5*, No. 8340.

(21) Kolle, M.; Salgard-Cunha, P. M.; Scherer, M. R. J.; Huang, F.; Vukusic, P.; Mahajan, S.; Baumberg, J. J.; Steiner, U. Mimicking the Colourful Wing Scale Structure of the Papilio Blumei Butterfly. *Nat. Nanotechnol.* **2010**, *5*, 511−515.

DOI: 10.1021/acsomega.8b01985
ACS Omega 2018, 3, 12089−12098

(22) Wendisch, F. J.; Oberreiter, R.; Salihovic, M.; Elsaesser, M. S.; Bourret, G. R. Confined Etching within 2D and 3D Colloidal Crystals for Tunable Nanostructured Templates: Local Environment Matters. *ACS Appl. Mater. Interfaces* **2017**, *9*, 3931−3939.
(23) Rey, B. M.; Elnathan, R.; Ditcovski, R.; Geisel, K.; Zanini, M.; Fernandez-Rodriguez, M. A.; Naik, V. V.; Frutiger, A.; Richtering, W.; Ellenbogen, T.; et al. Fully Tunable Silicon Nanowire Arrays Fabricated by Soft Nanoparticle Templating. *Nano Lett.* **2016**, *16*, 157−163.
(24) Honold, T.; Volk, K.; Rauh, A.; Fitzgerald, J. P. S.; Karg, M. Tunable Plasmonic Surfaces via Colloid Assembly. *J. Mater. Chem. C* **2015**, *3*, 11449−11457.
(25) Volk, K.; Fitzgerald, J. P. S.; Ruckdeschel, P.; Retsch, M.; König, T. A. F.; Karg, M. Reversible Tuning of Visible Wavelength Surface Lattice Resonances in Self-Assembled Hybrid Monolayers. *Adv. Opt. Mater.* **2017**, *5*, No. 1600971.
(26) Shumaker-Parry, J. S.; Rochholz, H.; Kreiter, M. Fabrication of Crescent-Shaped Optical Antennas. *Adv. Mater.* **2005**, *17*, 2131−2134.
(27) Haynes, C. L.; Van Duyne, R. P. Nanosphere Lithography: A Versatile Nanofabrication Tool for Studies of Size-Dependent Nanoparticle Optics. *J. Phys. Chem. B* **2001**, *105*, 5599−5611.
(28) Boechler, N.; Eliason, J. K.; Kumar, A.; Maznev, A. A.; Nelson, K. A.; Fang, N. Interaction of a Contact Resonance of Microspheres with Surface Acoustic Waves. *Phys. Rev. Lett.* **2013**, *111*, No. 036103.
(29) Khanolkar, A.; Wallen, S.; Abi Ghanem, M.; Jenks, J.; Vogel, N.; Boechler, N. A Self-Assembled Metamaterial for Lamb Waves. *Appl. Phys. Lett.* **2015**, *107*, No. 071903.
(30) Vega-Flick, A.; Duncan, R. A.; Wallen, S. P.; Boechler, N.; Stelling, C.; Retsch, M.; Alvarado-Gil, J. J.; Nelson, K. A.; Maznev, A. A. Contact-Based and Spheroidal Vibrational Modes of a Hexagonal Monolayer of Microspheres on a Substrate. *Wave Motion* **2018**, *76*, 122−133.
(31) Stelling, C.; Singh, C. R.; Karg, M.; König, T. A. F.; Thelakkat, M.; Retsch, M. Plasmonic Nanomeshes: Their Ambivalent Role as Transparent Electrodes in Organic Solar Cells. *Sci. Rep.* **2017**, *7*, No. 42530.
(32) Bley, K.; Semmler, J.; Rey, M.; Zhao, C.; Martic, N.; Klupp Taylor, R. N.; Stingl, M.; Vogel, N. Hierarchical Design of Metal Micro/Nanohole Array Films Optimizes Transparency and Haze Factor. *Adv. Funct. Mater.* **2018**, No. 1706965.
(33) Ho, Y.-H.; Chen, K. Y.; Liu, S. W.; Chang, Y. T.; Huang, D. W.; Wei, P. K. Transparent and Conductive Metallic Electrodes Fabricated by Using Nanosphere Lithography. *Org. Electron.* **2011**, *12*, 961−965.
(34) Wu, W.; Tassi, N. G. A Broadband Plasmonic Enhanced Transparent Conductor. *Nanoscale* **2014**, *6*, 7811−7816.
(35) Li, Y.; Zhang, J.; Zhu, S.; Dong, H.; Jia, F.; Wang, Z.; Sun, Z.; Zhang, L.; Li, Y.; Li, H.; et al. Biomimetic Surfaces for High-Performance Optics. *Adv. Mater.* **2009**, *21*, 4731−4734.
(36) Stelling, C.; Bernhardt, C.; Retsch, M. Subwavelength Etched Colloidal Monolayers: A Model System for Tunable Antireflective Coatings. *Macromol. Chem. Phys.* **2015**, *216*, 1682−1688.
(37) Vogel, N.; Belisle, R. A.; Hatton, B.; Wong, T. S.; Aizenberg, J. Transparency and Damage Tolerance of Patternable Omniphobic Lubricated Surfaces Based on Inverse Colloidal Monolayers. *Nat. Commun.* **2013**, *4*, No. 2167.
(38) Utech, S.; Bley, K.; Aizenberg, J.; Vogel, N. Tailoring Re-Entrant Geometry in Inverse Colloidal Monolayers to Control Surface Wettability. *J. Mater. Chem. A* **2016**, *4*, 6853−6859.
(39) Ellinas, K.; Tserepi, A.; Gogolides, E. From Superamphiphobic to Amphiphilic Polymeric Surfaces with Ordered Hierarchical Roughness Fabricated with Colloidal Lithography and Plasma Nanotexturing. *Langmuir* **2011**, *27*, 3960−3969.
(40) Min, W. L.; Jiang, B.; Jiang, P. Bioinspired Self-Cleaning Antireflection Coatings. *Adv. Mater.* **2008**, *20*, 3914−3918.
(41) Aveyard, R.; Clint, J. H.; Nees, D.; Paunov, V. N. Compression and Structure of Monolayers of Charged Latex Particles at Air / Water and Octane / Water Interfaces. *Langmuir* **2000**, *16*, 1969−1979.
(42) Vogel, N.; Retsch, M.; Fustin, C. A.; Del Campo, A.; Jonas, U. Advances in Colloidal Assembly: The Design of Structure and Hierarchy in Two and Three Dimensions. *Chem. Rev.* **2015**, *115*, 6265−6311.
(43) Isa, L.; Kumar, K.; Müller, M.; Grolig, J.; Textor, M.; Reimhult, E. Particle Lithography from Colloidal Self-Assembly at Liquid-Liquid Interfaces. *ACS Nano* **2010**, *4*, 5665−5670.
(44) Li, X.; Wang, T.; Zhang, J.; Yan, X.; Zhang, X.; Zhu, D.; Li, W.; Zhang, X.; Yang, B. Modulating Two-Dimensional Non-Close-Packed Colloidal Crystal Arrays by Deformable Soft Lithography. *Langmuir* **2010**, *26*, 2930−2936.
(45) Plettl, A.; Enderle, F.; Saitner, M.; Manzke, A.; Pfahler, C.; Wiedemann, S.; Ziemann, P. Non-Close-Packed Crystals from Self-Assembled Polystyrene Spheres by Isotropic Plasma Etching: Adding Flexibility to Colloid Lithography. *Adv. Funct. Mater.* **2009**, *19*, 3279−3284.
(46) Vogel, N.; Fernández-López, C.; Pérez-Juste, J.; Liz-Marzán, L. M.; Landfester, K.; Weiss, C. K. Ordered Arrays of Gold Nanostructures from Interfacially Assembled Au@ PNIPAM Hybrid Nanoparticles. *Langmuir* **2012**, *28*, 8985−8993.
(47) Jaber, S.; Karg, M.; Morfa, A.; Mulvaney, P. 2D Assembly of Gold-PNIPAM Core-Shell Nanocrystals. *Phys. Chem. Chem. Phys.* **2011**, *13*, 5576−5578.
(48) Geisel, K.; Isa, L.; Richtering, W. Unraveling the 3D Localization and Deformation of Responsive Microgels at Oil/water Interfaces: A Step Forward in Understanding Soft Emulsion Stabilizers. *Langmuir* **2012**, *28*, 15770−15776.
(49) Mehrabian, H.; Harting, J.; Snoeijer, J. H. Soft Particles at a Fluid Interface. *Soft Matter* **2016**, *12*, 1062−1073.
(50) Geisel, K.; Isa, L.; Richtering, W. The Compressibility of Ph-Sensitive Microgels at the Oil-Water Interface: Higher Charge Leads to Less Repulsion. *Angew. Chem., Int. Ed.* **2014**, *53*, 4905−4909.
(51) Style, R. W.; Isa, L.; Dufresne, E. R. Adsorption of Soft Particles at Fluid Interfaces. *Soft Matter* **2015**, *11*, 7412−7419.
(52) Scheidegger, L.; Fernández-Rodríguez, M. Á; Geisel, K.; Zanini, M.; Elnathan, R.; Richtering, W.; Isa, L. Compression and Deposition of Microgel Monolayers from Fluid Interfaces: Particle Size Effects on Interface Microstructure and Nanolithography. *Phys. Chem. Chem. Phys.* **2017**, *19*, 8671−8680.
(53) Rey, M.; Fernández-Rodríguez, M. Á; Steinacher, M.; Scheidegger, L.; Geisel, K.; Richtering, W.; Squires, T. M.; Isa, L. Isostructural Solid−solid Phase Transition in Monolayers of Soft Core−shell Particles at Fluid Interfaces: Structure and Mechanics. *Soft Matter* **2016**, *12*, 3545−3557.
(54) Rey, M.; Hou, X.; Tang, J. S. J.; Vogel, N. Interfacial Arrangement and Phase Transitions of PNiPAm Microgels with Different Crosslinking Density. *Soft Matter* **2017**, *13*, 8717−8727.
(55) Geisel, K.; Richtering, W.; Isa, L. Highly Ordered 2D Microgel Arrays: Compression versus Self-Assembly. *Soft Matter* **2014**, *10*, 7968.
(56) Picard, C.; Garrigue, P.; Tatry, M.-C.; Lapeyre, V.; Ravaine, S.; Schmitt, V.; Ravaine, V. Organization of Microgels at the Air-Water Interface under Compression: Role of Electrostatics and Cross-Linking Density. *Langmuir* **2017**, *33*, 7968−7981.
(57) Pinaud, F.; Geisel, K.; Massé, P.; Catargi, B.; Isa, L.; Richtering, W.; Ravaine, V.; Schmitt, V. Adsorption of Microgels at an Oil-Water Interface: Correlation between Packing and 2D Elasticity. *Soft Matter* **2014**, *10*, 6963−6974.
(58) Rauh, A.; Rey, M.; Barbera, L.; Zanini, M.; Karg, M.; Isa, L. Compression of Hard Core-Soft Shell Nanoparticles at Liquid-Liquid Interfaces: Influence of the Shell Thickness. *Soft Matter* **2016**, *13*, 158−169.
(59) Ciach, A.; Pękalski, J. Exactly Solvable Model for Self-Assembly of Hard Core-Soft Shell Particles at Interfaces. *Soft Matter* **2017**, *13*, 2603−2608.
(60) Vasudevan, S. A.; Rauh, A.; Barbera, L.; Karg, M.; Isa, L. Stable in Bulk and Aggregating at the Interface: Comparing Core-Shell

DOI: 10.1021/acsomega.8b01985
ACS Omega 2018, 3, 12089−12098

Nanoparticles in Suspension and at Fluid Interfaces. *Langmuir* **2018**, *34*, 886−895.
(61) Karg, M.; Wellert, S.; Prevost, S.; Schweins, R.; Dewhurst, C.; Liz-Marzán, L. M.; Hellweg, T. Well Defined Hybrid PNIPAM Core-Shell Microgels: Size Variation of the Silica Nanoparticle Core. *Colloid Polym. Sci.* **2011**, *289*, 699−709.
(62) Pelton, R. H.; Chibante, P. Preparation of Aqueous Latices with N-Isopropylacrylamide. *Colloids and Surfaces* **1986**, *20*, 247−256.
(63) Crocker, J. C.; Grier, D. G. When Like Charges Attract: The Effects of Geometrical Confinement on Long-Range Colloidal Interactions. *Phys. Rev. Lett.* **1996**, *77*, 1897−1900.
(64) Romanov, S. G.; Vogel, N.; Bley, K.; Landfester, K.; Weiss, C. K.; Orlov, S.; Korovin, A. V.; Chuiko, G. P.; Regensburger, A.; Romanova, A. S.; et al. Probing Guided Modes in a Monolayer Colloidal Crystal on a Flat Metal Film. *Phys. Rev. B* **2012**, *86*, No. 195145.
(65) Vogel, N.; Fischer, J.; Mohammadi, R.; Retsch, M.; Butt, H. J.; Landfester, K.; Weiss, C. K.; Kreiter, M. Plasmon Hybridization in Stacked Double Crescents Arrays Fabricated by Colloidal Lithography. *Nano Lett.* **2011**, *11*, 446−454.
(66) Han, H.; Huang, Z.; Lee, W. Metal-Assisted Chemical Etching of Silicon and Nanotechnology Applications. *Nano Today* **2014**, *9*, 271−304.
(67) Elnathan, R.; Delalat, B.; Brodoceanu, D.; Alhmoud, H.; Harding, F. J.; Buehler, K.; Nelson, A.; Isa, L.; Kraus, T.; Voelcker, N. H. Maximizing Transfection Efficiency of Vertically Aligned Silicon Nanowire Arrays. *Adv. Funct. Mater.* **2015**, *25*, 7215−7225.
(68) Elnathan, R.; Isa, L.; Brodoceanu, D.; Nelson, A.; Harding, F. J.; Delalat, B.; Kraus, T.; Voelcker, N. H. Versatile Particle-Based Route to Engineer Vertically Aligned Silicon Nanowire Arrays and Nanoscale Pores. *ACS Appl. Mater. Interfaces* **2015**, *7*, 23717−23724.
(69) Stöber, W.; Fink, A.; Bohn, E. Controlled Growth of Monodisperse Silica Spheres in the Micron Size Range. *J. Colloid Interface Sci.* **1968**, *26*, 62−69.
(70) Rauh, A.; Rey, M.; Barbera, L.; Zanini, M.; Karg, M.; Isa, L. Compression of Hard Core−soft Shell Nanoparticles at Liquid−liquid Interfaces: Influence of the Shell Thickness. *Soft Matter* **2017**, *13*, 158−169.
(71) Parnell, S. R.; Washington, A. L.; Parnell, A. J.; Walsh, A.; Dalgliesh, R. M.; Li, F.; Hamilton, W. A.; Prevost, S.; Fairclough, J. P. A.; Pynn, R. Porosity of Silica Stöber Particles Determined by Spin-Echo Small Angle Neutron Scattering. *Soft Matter* **2016**, *12*, 4709−4714.
(72) Huang, Z.; Geyer, N.; Werner, P.; De Boor, J.; Gösele, U. Metal-Assisted Chemical Etching of Silicon: A Review. *Adv. Mater.* **2011**, *23*, 285−308.

DOI: 10.1021/acsomega.8b01985
ACS Omega 2018, 3, 12089−12098